Chaos-induced intensification of wave scattering

I. P. Smirnov and A. L. Virovlyansky
Institute of Applied Physics, Russian Academy of Science, 46 Ul'yanov Street, 603950 Nizhny Novgorod, Russia

M. Edelman
Courant Institute of Mathematical Sciences, New York University 251 Mercer Street, New York, New York 10012, USA

G. M. Zaslavsky
Courant Institute of Mathematical Sciences, New York University 251 Mercer Street, New York, New York 10012, USA
and Department of Physics, New York University 2-4 Washington Place, New York, New York 10003, USA
(Received 15 February 2005; revised manuscript received 2 June 2005; published 15 August 2005)

Sound-wave propagation in a strongly idealized model of the deep-water acoustic waveguide with a periodic range dependence is considered. It is investigated how the phenomenon of ray and wave chaos affects the sound scattering at a strong mesoscale inhomogeneity of the refractive index caused by the synoptic eddy. Methods derived in the theory of dynamical and quantum chaos are applied. When studying the properties of wave chaos we decompose the wave field into a sum of Floquet modes analogous to quantum states with fixed quasienergies. It is demonstrated numerically that the "stable islands" from the phase portrait of the ray system reveal themselves in the coarse-grained Wigner functions of individual Floquet modes. A perturbation theory has been derived which gives an insight into the role of the mode-medium resonance in the formation of Floquet modes. It is shown that the presence of a weak internal-wave-induced perturbation giving rise to ray and wave chaos strongly increases the sensitivity of the monochromatic wave field to an appearance of the eddy. To investigate the sensitivity of the transient wave field we have considered variations of the ray travel times—arrival times of sound pulses coming to the receiver through individual ray paths—caused by the eddy. It turns out that even under conditions of ray chaos these variations are relatively predictable. This result suggests that the influence of chaotic-ray motion may be partially suppressed by using pulse signals. However, the relative predictability of travel time variations caused by a large-scale inhomogeneity is not a general property of the ray chaos. This statement is illustrated numerically by considering an inhomogeneity in the form of a perfectly reflecting bar.

DOI: 10.1103/PhysRevE.72.026206 PACS number(s): 05.45.Mt, 05.45.Pq, 43.30.+m

I. INTRODUCTION

In the past two decades it has been realized that chaotic behavior is a generic property of sound rays in range-dependent underwater acoustic waveguides [1–8]. The ray chaos in the ocean is caused by a weak perturbation of the refractive index due to internal waves. In the presence of this perturbation the ray paths become extremely sensitive to variations of the initial conditions: the vertical separation between the paths with close starting parameters, on the average, grows with range r as $\exp(\lambda r)$, where λ is the Lyapunov exponent. For realistic models of deep-water waveguides the values of λ are on the order of 100 km [9,10]. At ranges $O(1000$ km) the ray chaos is well developed and it cannot be ignored when describing long-range sound propagation in the ocean [9,11–15]. The manifestation of chaotic ray motion at a finite wavelength is called wave chaos. It has a well-known prototype in quantum theory called quantum chaos [16–18].

In the present paper our main objective is to investigate how the phenomenon of ray and wave chaos affects the sound scattering at a strong inhomogeneity of the refractive index with comparatively large spatial scales. In underwater acoustics this problem is of current importance. The point is that besides internal-wave-induced perturbations in oceanic acoustic waveguides there exist so-called mesoscale inhomogeneities whose horizontal scales range from tens to hundreds kilometers and which evolve on time scales of 1 month. The corresponding vertical scales vary from 100 m to 1 km [19,20]. In contrast, the internal waves are characterized by horizontal spatial scales ranging from hundreds meters to tens of kilometers and vertical scales of tens of meters. Their temporal scales are on the order of hours. It should be emphasized that the sound speed variations (they are proportional to temperature variations) associated with mesoscale inhomogeneities usually are significantly stronger than those caused by internal waves. The reconstruction of mesoscale inhomogeneities is an important problem of acoustic monitoring aimed at investigation of the temperature field of the ocean [21]. From the viewpoint of solving inverse problems it is essential to understand how a mesoscale inhomogeneity affects the properties of ray and wave chaos.

In describing sound-wave propagation we shall neglect horizontal refraction. This assumption is widely used in underwater acoustics because the cross-range gradients of the sound speed are typically two orders of magnitude smaller than the vertical gradients. That is why the sound propagation is well described as two dimensional (having no out-of-plane scattering) [9,22] and the sound speed c in this model depends only on the range r and depth z. In our environmental model the sound speed field is presented in the form

$$c(r,z) = \bar{c}(z) + \delta c_{\mathrm{iw}}(r,z) + \delta c_{\mathrm{meso}}(r,z), \quad (1)$$

where $\bar{c}(z)$ is a smooth range-independent profile, $\delta c_{\mathrm{iw}}(r,z)$ is a weak perturbation induced by internal waves and giving rise to ray chaos, and $\delta c_{\mathrm{meso}}(r,z)$ is a mesoscale inhomogeneity. Let us emphasize that the function $\delta c_{\mathrm{meso}}(r,z)$, determining our scatterer, is assumed to be smooth and in the absence of internal waves the ray trajectories remain regular. This assumption implies that we do not deal with chaotic scattering. The latter takes place when the scatterer has a so complicated a structure that the ray dynamics within the scattering region becomes chaotic [23,24].

In what follows we shall consider a perturbation $\delta c_{\mathrm{meso}}(r,z)$ modeling a synoptic eddy. Such eddies are observed near intensive currents such as the Gulf Stream, and they are formed as a result of the separation of great meanders from the main flow [19]. Although the internal-wave-induced perturbation $\delta c_{\mathrm{iw}}(r,z)$ is weak and it cannot significantly affect the ray paths while the latter are crossing the eddy, the influence of this perturbation may be great. In the presence of $\delta c_{\mathrm{iw}}(r,z)$ the variations of trajectories caused by the eddy will be strongly "amplified" at ranges exceeding λ^{-1} due to chaotic ray instability. In this sense, the presence of internal waves makes the ray structure of the wave field much more sensitive to the mesoscale inhomogeneity. Our task in the present paper is to investigate how the perturbation $\delta c_{\mathrm{iw}}(r,z)$ affects the sensitivity of the wave field at a finite wavelength.

To simplify the analysis we exploit a highly idealized model of the internal-wave-induced perturbation with a periodic range dependence, borrowed from Ref. [3]. It has been used in a series of our recent papers [25–27] where the effects caused by the coexistence of chaotic and regular rays have been considered. Although this model is somewhat artificial, it provides a good starting point for both ray-based and wave-based analyses of an irregular structure of the wave field. The fact is that in the parabolic equation approximation the sound-wave field is governed by the same parabolic (Schrödinger) equation as the wave function of a nonlinear oscillator driven by an external periodic force [28,29]. Therefore we can use methods from the theory of dynamical and wave chaos where the behavior of the nonlinear oscillator has been studied extensively. In particular, we shall apply the Poincaré map, which allows one to explore the phase space of the ray system and find areas visited by predominantly chaotic ("chaotic sea") or predominantly regular ("stable islands") trajectories [1–3]. Due to periodicity of the external perturbation, our waveguide is an analog of the quantum Floquet system. Correspondingly, its description becomes especially simple if the wave field is decomposed into a sum of the Floquet modes representing analogs of the quantum states with fixed quasienergies [16,18,30].

The Floquet modes provide a remarkably simple description of the monochromatic wave field in our environmental model in the absence of the eddy. It is shown that the characteristic features of the phase space of the ray system (stable islands and chaotic sea) reveal themselves in the structures of individual modes. It turns out that all Floquet modes may be divided into "chaotic" and "regular" ones describing constituents of the wave field formed by contributions from predominantly chaotic and predominantly regular rays, respectively. We have derived a simple perturbation theory that establishes, analytically, the connection between the Floquet modes and modes of the unperturbed waveguide with $c(r,z)=\bar{c}(z)$.

In order to compare the sensitivity of the monochromatic wave field to the mesoscale inhomogeneity in the presence and absence of internal waves we have simulated scattering of the Floquet modes and modes of the unperturbed waveguide at the eddy. It has been found that the coupling of Floquet modes is much more strong. This means that chaos magnifies the sensitivity of the wave field not only in the geometrical optics limit but at a finite wavelength as well.

In order to investigate the sensitivity of the transient wave field we have considered variations of the ray travel times—arrival times of sound pulses coming to the receiver through individual ray paths—caused by the eddy. These characteristics are important from the viewpoint of applications because, so far, the ray travel time has been the main signal parameter in the underwater acoustics experiments from which inversions have been performed to reconstruct the ocean temperature field [21,31,32]. Our attention has been restricted to the so-called time fronts representing ray arrivals in the time-depth plane. In underwater acoustics it is well known that some segments of the time front may exhibit comparatively low sensitivity to the medium inhomogeneities giving rise to ray chaos [9,10,12,33,34]. Our simulations have shown that this comparatively low sensitivity remains in the presence of the mesoscale inhomogeneity. However, it should be emphasized that this property is not general and the chaotic time front may be very sensitive to large-scale inhomogeneities of other types. This statement is illustrated with a numeric example.

The paper is organized as follows. In Sec. II we describe our environmental model and present standard formulas that determine the ray and mode representations of the wave field. The ray representation is formulated using the Hamiltonian formalism in terms of momentum-position and action-angle canonical variables. In this section the Floquet modes are introduced. Analysis of their properties is a subject of Sec. III. In order to link the Floquet modes to the phase portrait of the ray system constructed using the Poincaré map, the Husimi distributions of modes are evaluated. The connection between structures of the Husimi functions and the phase portrait of the ray system constructed using the Poincaré map is discussed. An approximate analytical expression for the Floquet modes is derived using a perturbation theory. The manifestation of the mode-medium resonance in the structure of individual Floquet modes and in the wave-field decomposition into a sum of modes of the unperturbed waveguide is studied. In Sec. IV we investigate the mode coupling due to scattering at the synoptic eddy. The main objective of this study is to find out how the presence of a weak internal-wave-induced perturbation affects the mode coupling. Similarly, in Sec. V we study how this perturbation affects the timefront in the presence of the eddy. In Sec. VI the results of this work are summarized.

II. RAY AND MODE REPRESENTATIONS OF THE WAVE FIELD

A. Mathematical model of an underwater acoustic waveguide

Consider a monochromatic wave field at a carrier frequency f in a two-dimensional acoustic waveguide with the sound speed c being a function of depth z and range r. We shall assume that at each range point the sound speed profile has a single minimum. The wave field $u(r,z)$ is governed by the Helmholtz equation [19,35,36]

$$\frac{1}{r}\frac{\partial}{\partial r}r\frac{\partial u}{\partial r}+\frac{\partial^2 u}{\partial z^2}+\frac{\Omega^2}{c^2(r,z)}u=0, \tag{2}$$

where $\Omega=2\pi f$. Select a reference sound speed c_0 such that $|c(r,z)-c_0|\ll c_0$ (in underwater acoustics such a choice of c_0 is always possible) and assume that the grazing angles of propagating waves are small. Then it is convenient to introduce an envelope function $v(r,z)$ connected to $u(r,z)$ by an expression

$$u=\frac{v}{\sqrt{r}}e^{ikr}, \tag{3}$$

with $k=\Omega/c_0$. This function is approximately described by the standard parabolic equation [9,19,36]

$$2ik\frac{\partial v}{\partial r}+\frac{\partial^2 v}{\partial z^2}-2k^2Uv=0, \tag{4}$$

where

$$U(r,z)=\frac{1}{2}\left(1-\frac{c_0^2}{c^2(r,z)}\right). \tag{5}$$

Notice that Eq. (4) formally coincides with the time-dependent Schrödinger equation. In this analogy r,k^{-1}, and $U(r,z)$ play roles of time, Planck's constant, and potential, respectively.

In what follows we consider the sound speed field (1) with $\bar{c}(z)$ taken in the form of the Munk profile [19,22]:

$$\bar{c}(z)=c_0[1+\varepsilon(e^{-\eta}+\eta-1)],\quad \eta=2(z-z_a)/B, \tag{6}$$

where $c_0=1.5$ km/s, $z_a=1$ km is the sound channel axis (depth corresponding to the minimum of sound speed), $\varepsilon=0.0057$, and $B=1$ km. It is assumed that the z axis is directed downwards and $z=0$ corresponds to the water surface.

Following Refs. [3,25–27,37] we choose a perturbation

$$\delta c_{\mathrm{iw}}(r,z)=-2\gamma\, c_0\frac{z}{B}e^{2z/B}\sin(2\pi r/L), \tag{7}$$

where $\gamma=0.01$ and the spatial period $L=10$ km. The upper panel of Fig. 1 presents the unperturbed profile $\bar{c}(z)$ (solid line) and maximal deviations due to the perturbation δc_{iw} (dashed lines).

The mesoscale inhomogeneity modeling the sound speed inhomogeneity caused by a synoptic eddy is determined by the relation (the model is borrowed from Ref. [38])

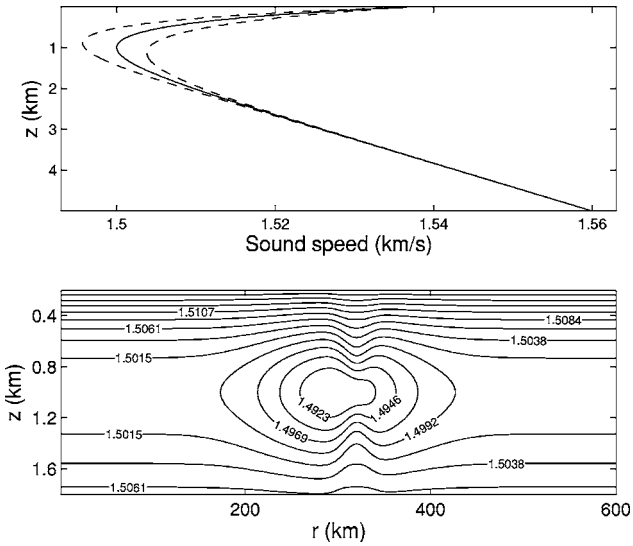

FIG. 1. *Upper panel*: unperturbed sound speed profile $\bar{c}(z)$ (solid line) and its maximal deviations (dashed line) due to the perturbation δc_{iw}. *Lower panel*: sound speed field modelling a synoptic eddy in a deep sea. Contour labels are of sound speed in km/s.

$$\delta c_{\mathrm{meso}}(r,z)=c_1\exp\left(-\frac{(r-r_1)^2}{\Delta r^2}-\frac{(z-z_1)^2}{\Delta z(r)^2}\right), \tag{8}$$

where

$$\Delta z(r)=\Delta z_c-\Delta z_v\exp\left(-\frac{(r-r_v)^2}{\Delta r_v}\right). \tag{9}$$

The following values of parameters have been selected: $c_1=-0.01$ km/s, $z_1=1$ km, $\Delta r=80$ km, $\Delta z_c=0.5$ km, $\Delta z_v=0.25$ km, $r_v=320$ km, and $\Delta r_v=20$ km. The isolines of the total sound field for $r_1=300$ km are shown in the lower panel of Fig. 1.

Our choice of a weak perturbation $\delta c_{\mathrm{iw}}(r,z)$ needs a comment. The amplitude of δc takes its maximum value of about 5 m/s at 500 m depth (see Fig. 1). Although both the range and depth dependences of δc_{iw} differ from those observed in experiments [22], our highly idealized perturbation gives rise to a chaotic-ray motion whose properties resemble that found in more realistic environmental models [9,10,12]. For example, travel times of chaotic rays in a waveguide determined by Eqs. (1)–(7) form rather compact clusters [26]. It also should be mentioned that the Lyapunov exponents characterizing stochastic instability of chaotic ray paths in our model are approximately the same (about 0.01 km^{-1} [25]) as in a typical deep-water waveguide with internal-wave-induced inhomogeneities [9,10]. Besides, the expression (7) is so simple that it can be used not only in numerical simulations but even in obtaining analytical estimates [27]. An important advantage of our perturbation is its periodic range dependence which allows one to apply the Poincaré map for investigating the structure of the phase space and to introduce the Floquet modes for investigating the structure of the wave field at a finite wavelength. These options will be used in Secs. III and IV.

B. Hamiltonian formalism for a description of the ray dynamics

1. Position-momentum variables

In the geometrical optics approximation the wave field is formed by contributions from all rays arriving at the observation point. The ray trajectory is defined by the Hamilton equations [1,9]

$$\frac{dz}{dr} = \frac{\partial H}{\partial p}, \quad \frac{dp}{dr} = -\frac{\partial H}{\partial z}, \tag{10}$$

with the Hamiltonian

$$H = p^2/2 + U. \tag{11}$$

The momentum p is connected to the ray grazing angle χ through the relation

$$p = dz/dr = \tan \chi. \tag{12}$$

A contribution to the wave field from an individual ray is presented in the form

$$v = Ae^{ikS}, \tag{13}$$

where S and A are the ray eikonal and amplitude, respectively. The eikonal S is an analog to Hamilton's principal function in classical mechanics, and it is given by an integral

$$S = \int (pdz - Hdr) \tag{14}$$

running over the ray path [9,39,40]. The ray amplitude A is expressed through parameters of the ray trajectory [9,41] but in the present paper the corresponding formula will not be used.

A pulse signal $\tilde{v}(r,z,t)$ arriving at the point (r,z) via a particular ray path can be synthesized by integrating Eq. (13) over the carrier frequency f. This yields

$$\tilde{v}(r,z,t) = \int df\, A(r,z)Q(f)\exp\left[2\pi if\left(\frac{r}{c_0} + \frac{1}{c_0}S(z,r) - t\right)\right], \tag{15}$$

where the factor $Q(f)$ is proportional to the spectrum of an initially emitted signal. The quantity

$$T = \frac{r}{c_r} + \frac{1}{c_r}S(z,r) \tag{16}$$

describes the time delay of a pulse coming to the receiver through an individual ray path and is called the ray travel time.

2. Action-angle variables

Since ray trajectories in the waveguide are oscillating curves, their analysis may be simplified by using the so-called action-angle variables [1,39]. In mechanics the latter are often applied to study oscillations of particles in potential wells. To introduce these variables, first, consider a range-independent waveguide where the Hamiltonian H remains constant along the ray path (analog to the energy conservation law in mechanics). The action variable I is defined by the integral [1,39]

$$I = \frac{1}{2\pi}\oint p\, dz = \frac{1}{\pi}\int_{z_{\min}}^{z_{\max}} dz\sqrt{2[H - U(z)]}, \tag{17}$$

where $z_{\min}$ and $z_{\max}$ are the lower and upper-ray turning depths, respectively, satisfying the condition $U(z)=H$. Equation (17) defines the "energy" H as a function of the action I. The ray trajectory is a periodic curve whose period along the r axis (the cycle length), R, and the angular frequency of spatial oscillations, ω, are determined by the relation

$$\frac{dH}{dI} = \omega = \frac{2\pi}{R}. \tag{18}$$

Take one cycle of the unperturbed ray path that begins at the minimum of the trajectory. At the first half-cycle the canonical transformation

$$p = p(I,\theta), \quad z = z(I,\theta), \tag{19}$$

from the position momentum, (p,z), to the action-angle, (I,θ), variables is determined by the equations [1,4,39]

$$p = \frac{\partial G}{\partial z}, \quad \theta = \frac{\partial G}{\partial I}, \tag{20}$$

with

$$G(I,z) = \int_{z_{\min}}^{z} dz\sqrt{2[H(I) - U(z)]} \tag{21}$$

being a generating function of the canonical transformation. At this half-cycle the angle variable θ varies from 0 to π. The transformation is continued to the next half-cycle ($\pi < \theta < 2\pi$) using the relations $p(I,\theta) = -p(I,2\pi - \theta)$ and $z(I,\theta) = z(I,2\pi - \theta)$. The ray equations in the new variables take the trivial form

$$\frac{dI}{dr} = -\frac{\partial H}{\partial \theta} = 0, \quad \frac{d\theta}{dr} = \frac{\partial H}{\partial I} = \omega(I). \tag{22}$$

Note that the so-defined angle variable θ varies from 0 to 2π at a part of the trajectory beginning at one minimum and ending at the next one. To make the angle variable continuous, its value should be increased by 2π at the beginning of each new cycle. Both functions in Eq. (19) are periodic in θ with period 2π. Correspondingly, an arbitrary function $N(z)$ expressed through the action-angle variables becomes a periodic function of θ and can be expanded in a Fourier series

$$N[z(I,\theta)] = \sum_{\nu=0}^{\infty} N_\nu(I)\cos(\nu\theta). \tag{23}$$

The coefficients $N_\nu(I)$ are expressed analytically only for a few special examples of $U(z)$ and $N(z)$. But numerical evaluation of these coefficients can be easily performed using a standard ray code. If we denote the ray trajectory with the action variable I by $z(r)$, then

$$N_\nu(I) = \frac{q_\nu}{R(I)} \int_0^{R(I)} dr\ N[z(r_{\min}+r)]\cos[\nu\omega(I)(r_{\min}+r)], \tag{24}$$

where $q_0=1$, $q_\nu=2$ for $\nu>0$, and $r_{\min}$ is a range corresponding to a minimum of the ray path.

C. Normal modes of the range-independent waveguide

1. Eigenfunctions and eigenvalues in the WKB approximation

Consider the unperturbed waveguide with sound speed field $c(r,z)=\bar{c}(z)$. The normal-mode representation of the wave field in this range-independent waveguide is given by an expansion into a sum of eigenfunctions of the Sturm-Liouville eigenvalue problem [35,42],

$$\frac{1}{2}\frac{d^2\varphi_m}{dz^2} + k^2(E_m - \bar{U})\varphi_m = 0, \tag{25}$$

with appropriate boundary conditions. The "potential" $\bar{U}(z)$ is defined by Eq. (5) with $c(r,z)$ replaced by $\bar{c}(z)$. The boundary conditions can be determined by reflection coefficients at the surface, $V_s=e^{i\phi_s}$, and at the bottom, $V_b=e^{i\phi_b}$. We assume that reflections at boundaries occur without energy loss, and therefore ϕ_s and ϕ_b are real constants. In particular, for a pressure release surface and rigid bottom we have $\phi_s=\pi$ and $\phi_b=0$. In the case when the upper (lower) mode turning points lie within a water bulk we have $\phi_s=-\pi/2$ ($\phi_b=-\pi/2$). The eigenfunctions are orthogonal and normalized in such a way that

$$\int dz\ \varphi_m\varphi_n = \delta_{mn}. \tag{26}$$

The eigenfunctions $\varphi_m(z)$ and eigenvalues E_m can be easily found numerically using a standard-mode code [36]. An analytical description can be obtained in the WKB approximation [19,42]. For the eigenvalue of the mth mode it yields

$$E_m = H(I_m), \tag{27}$$

where I_m satisfies the quantization rule

$$kI_m = m - \frac{\phi_s+\phi_b}{2\pi}. \tag{28}$$

The quantity I_m can be treated as an action variable associated with the mth mode: if only this mode is excited, then all rays have the same action $I=I_m$. Using Eq. (18) we get a simple approximate relation for the difference between eigenvalues of neighboring modes [19],

$$\frac{dE_m}{dm} = E_{m+1} - E_m = \frac{2\pi}{kR_m}, \tag{29}$$

where $R_m \equiv 2\pi/\omega(I_m)$ is the cycle length of a ray with an action variable $I=I_m$.

The mth eigenfunction $\varphi_m(z)$ between its turning points can be represented as [42]

$$\varphi_m(z) = \varphi_m^+(z) + \varphi_m^-(z), \tag{30}$$

where

$$\varphi_m^\pm(z) = Q_m e^{\pm i[kS_m(z)+\phi_b/2)]}, \tag{31}$$

$$S_m(z) = \int_{z_{\min}}^{z} dz\ p_m(z), \quad p_m(z) = \sqrt{2[E_m - U(z)]}, \tag{32}$$

and

$$Q_m = \sqrt{\frac{\omega_m}{2\pi p_m(z)}}. \tag{33}$$

Since the eigenfunctions $\varphi_m(z)$ form a complete set, the wave field can be decomposed into the sum

$$u(r,z) = \sum_m B_m(r)\varphi_m(z). \tag{34}$$

In the range-independent waveguide with $c(r,z)=\bar{c}(z)$,

$$B_m(r) = e^{-ikE_m r}B_m(0). \tag{35}$$

2. Matrix elements

In the WKB approximation the matrix element of a smooth function $N(z)$ [42],

$$N_{m\nu} = \int dz\ \varphi_m(z)N(z)\varphi_\nu(z), \tag{36}$$

can be expressed through coefficients of expansion (23). Indeed, take $N(z)$ whose characteristic scale is large compared to the wavelength $2\pi/k$. Since $\varphi_m(z)$ are rapidly oscillating functions of z, the matrix elements are very small unless m and ν are close. Making use of Eqs. (30)–(32) rewrite Eq. (36) in the form

$$N_{m,m+\Delta m} = 2\int_{z_{\min}}^{z_{\max}} dz\ N(z)Q_m^2(z)\cos\{k[S_{m+\Delta m}(z) - S_m(z)]\}. \tag{37}$$

From Eqs. (29) and (32) it follows that

$$k[S_{m+\Delta m}(z) - S_m(z)] = \omega_m \Delta m \int_{z_{\min}}^{z} \frac{dz}{p_m(z)}. \tag{38}$$

According to Eq. (12), $dz/p_m=dr$ and the integral on the right can be considered as a shift along the r axis between a minimum and a current point of a ray trajectory with action I_m. In the range-independent waveguide $\omega_m r=\theta$ and we get a desired connection between the matrix elements and the coefficients of Eq. (23):

$$N_{m,m+\Delta m} = \frac{1}{2\pi}\int_0^{2\pi} d\theta\ N[z(I_m,\theta)]\cos(\Delta m\ \theta) = \frac{1}{2}N_{|\Delta m|}(I_m). \tag{39}$$

D. Floquet modes of periodic waveguide

The Floquet theorem allows one to extend the concept of normal modes to the case of a waveguide with periodic range dependence [16,18]. In our model, in the absence of the eddy,

$$c(r,z) = \bar{c}(z) + \delta c_{\mathrm{iw}}(r,z) \tag{40}$$

and the sound speed field is a periodic function of r. Then the solution of Eq. (4) can be presented as a sum of Floquet modes

$$u_m(r,z) = e^{i\alpha_m r/L}\Psi_m(r,z), \tag{41}$$

where $\Psi_m(r+L,z)=\Psi_m(r,z)$, α_m are real constants, and $m=0, 1,\ldots$. In quantum mechanics analogous terms describe the so-called Floquet states and constants α_m are proportional to their quasienergies. $u_m(r,z)$ are eigenfunctions of the shift operator $\hat{F}$,

$$\hat{F}u_m(r,z) = u_m(r+L,z) = e^{i\alpha_m}u_m(r,z). \tag{42}$$

Since the shift operator is Hermitian, $\Psi_m(r,z)$ form a complete orthonormal set [16,18].

Let us consider the functions

$$\psi_m(z) \equiv \Psi_m(0,z) \tag{43}$$

and present each of them as a decomposition

$$\psi_m(z) = \sum_q C_{qm}\varphi_q(z). \tag{44}$$

To number the Floquet modes we shall associate a parameter μ with each function $\psi_m(z)$, where

$$\mu = \sum_q q|C_{qm}|^2, \tag{45}$$

and sort the Floquet modes in the order of increasing values of μ. A more detailed description of the numbering is given below in Sec. III C. Here we only note that the eigenfunctions $\psi_m(z)$ with small numbers m describe waves localized at depths z in the vicinity of the minimum of $U(0,z)$. The greater is the number m, the steeper are the grazing angles of waves forming the corresponding Floquet mode.

Consider a unitary Floquet matrix F with elements

$$F_{mn} = \int dz\ \varphi_m(z)\hat{F}\varphi_n(z), \tag{46}$$

where $\hat{F}\varphi_n(z)$ denotes a solution to the parabolic equation (4) at range $r=L$ obtained for an initial condition $u(0,z)=\varphi_n(z)$. In our simulations we have solved Eq. (4) using the code MMPE [43]. Substituting Eq. (44) into Eq. (42) with $r=0$ it is easy to see that eigenvalues β_m and eigenvectors $\mathbf{X}_m$ of matrix F, satisfying the equation

$$F\mathbf{X}_m = \beta_m\mathbf{X}_m, \tag{47}$$

determine the connection between the modes of the unperturbed waveguide and the Floquet ones: namely,

$$\beta_m = e^{i\alpha_m}$$

and components of the mth eigenvector $\mathbf{X}_m$ are $(C_{1m}, C_{2m}, \ldots)$.

Using the Floquet modes yields a simple expression for cross sections of the wave field at discrete ranges nL in the form of a decomposition

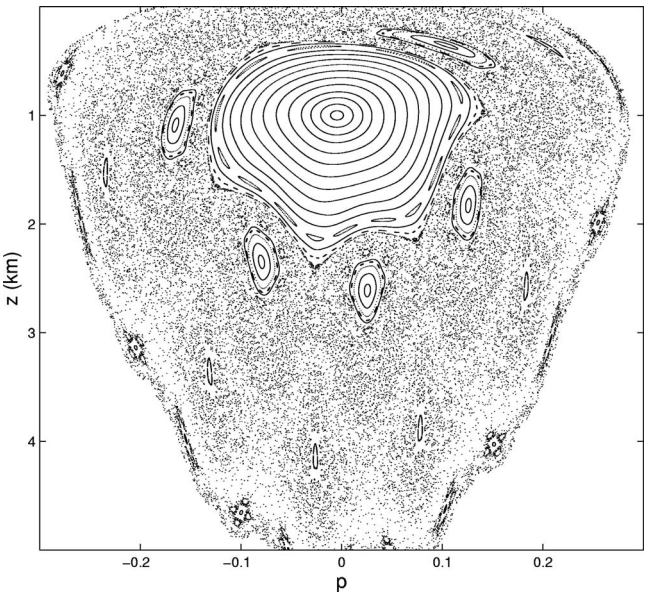

FIG. 2. Phase portrait of the ray system.

$$u(nL,z) = \sum_m G_m(n)\psi_m(z), \tag{48}$$

where

$$G_m(n) = e^{in\alpha_m}G_m(0). \tag{49}$$

At any intermediate range a similar decomposition is valid with the same α_m but different eigenfunctions $\psi_m(z)$. Equation (48) may be considered as an analog of Eq. (34) for a waveguide with periodic range dependence.

III. "REGULAR" AND "IRREGULAR" CONSTITUENTS OF THE WAVE FIELD

A. Phase portrait

As has been shown in Refs. [3,25–27,37] the perturbation δc_{iw} gives rise to ray chaos. This is clearly seen in Fig. 2 representing the phase portrait of our ray system constructed using the Poincaré map [1–5],

$$(p_{n+1}, z_{n+1}) = \hat{T}(p_n, z_n), \tag{50}$$

where a symbol $\hat{T}$ denotes transformation of the momentum and coordinate of a ray trajectory taken at range nL to range $(n+1)L$ for $n=0, 1,\ldots$. We see a typical picture of stable islands formed by regular curves submerged in a chaotic sea filled with randomly scattered points depicting chaotic rays. The islands and chaotic sea show areas in the phase space visited by predominantly regular and chaotic rays, respectively.

B. Manifestations of stable islands and chaotic sea in Floquet modes

In order to link the structure of the Floquet mode with the classical phase space we shall consider the Wigner function defined by the relation

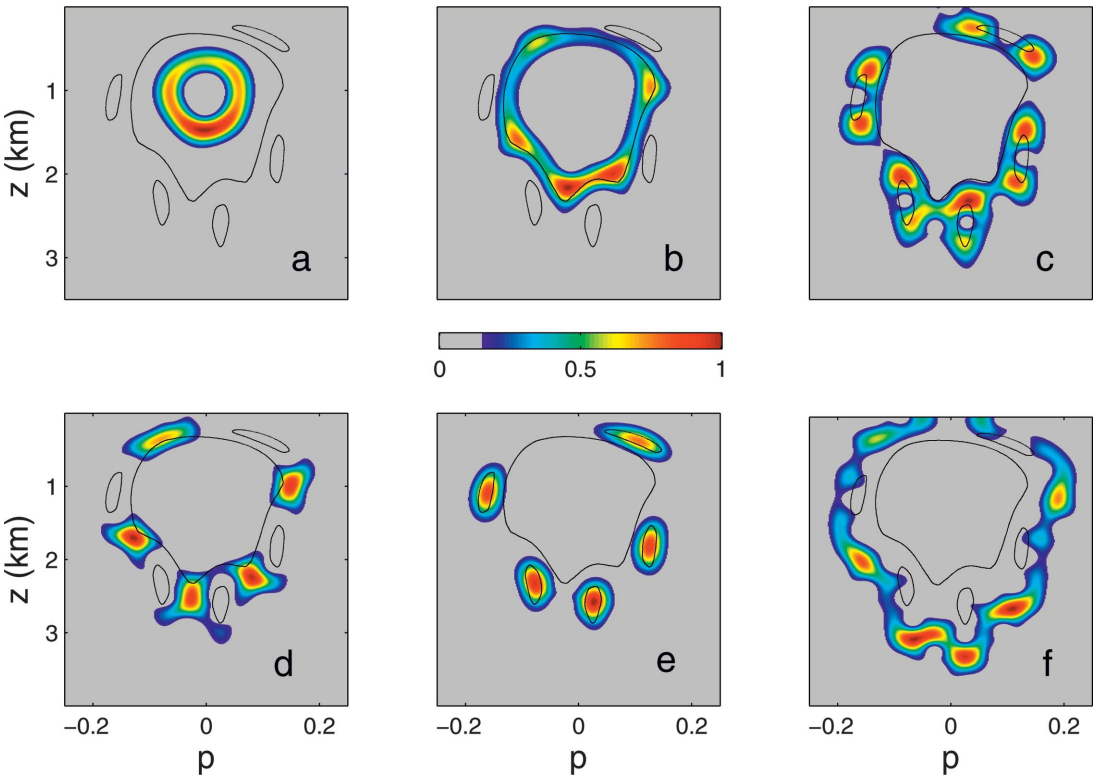

FIG. 3. (Color) Husimi distributions for the Floquet eigenfunctions $\psi_5(z)$ (a), $\psi_{18}(z)$ (b), $\psi_{24}(z)$ (c), $\psi_{25}(z)$ (d), $\psi_{30}(z)$ (e), and $\psi_{45}(z)$ (f).

$$W_m(p,z) = \frac{k}{2\pi}\int d\zeta \psi_m(z-\zeta/2)\psi_m^*(z+\zeta/2)e^{ikp\zeta}, \quad (51)$$

where the asterisk denotes the complex conjugation. Equation (51) can be interpreted as an amplitude of a plane wave propagating at the grazing angle $\theta=\arctan p$ with respect to the r axis. Thus, the Wigner function dependence on momentum p in wave theory characterizes a local angular structure of the wave field. To smooth out small-scale features of this structure and make large-scale ones more noticeable we shall use a coarse-grained Wigner function [44]

$$w_m(p,z) = \frac{1}{2\pi}\int dz'dp' e^{-(z-z')^2/2\Delta_z^2-(p-p')^2/2\Delta_p^2} W_m(p',z'). \quad (52)$$

Selecting the smoothing scales satisfying the condition $\Delta_z\Delta_p=1/2k$ we arrive at the Husimi distribution function [16,45]: after some algebra Eq. (52) reduces to

$$w_m(p,z) = \left| \frac{1}{\sqrt[4]{2\pi\Delta_z^2}}\int dz' \psi_m(z') \times \exp\left[ikp(z'-z) - \frac{(z'-z)^2}{4\Delta_z^2}\right]\right|^2. \quad (53)$$

Thus, $w_m(p,z)$ represents a projection of the wave field onto a Gaussian state with minimum uncertainty (coherent state) centered at a point (p,z).

Our attention will be restricted to Husimi distributions of eigenfunctions $\psi_m(z)$ corresponding to different Floquet modes. Note that $\psi_m(z)$ describe the stroboscopic observations of the Floquet modes at the same range points nL (n is an integer) which have been used for construction of the phase portrait shown in Fig. 2. All numerical results presented in this paper have been obtained for a carrier frequency $f=75$ Hz. We have computed the Floquet modes with numbers $m\leqslant 60$.

Note that our Hamiltonian system determining the ray motion has a mixed phase space, where regular and chaotic regions coexist. The results presented in Fig. 3 suggest that chaotic and regular rays contribute to different Floquet modes. This figure shows Husimi functions evaluated for six Floquet modes with $\Delta_z=0.1$ km. These examples have been selected (out of the first 60 modes considered in our numerical simulations) to demonstrate a variety of structures of Floquet modes in the environmental model determined by Eqs. (6) and (7). At each panel we have outlined borders of the central island and five subislands surrounding it. Although the range variations of the sound speed are most pronounced at its minimum (see Fig. 1), the first Floquet eigenfunctions $\psi_m(z)$ are closest to their unperturbed counterparts—i.e., to functions $\varphi_m(z)$ with the same numbers m. Using the WKB approximation it is easy to demonstrate that the Husimi function for any $\varphi_m(z)$ is localized in the vicinity of a closed curve defined by equation $p=\pm p_m(z)$ and representing a period of an unperturbed ray (in the phase plane) corresponding to the given mode. It can be said that the Husimi function is a fuzzy version of this closed curve. An example is shown in

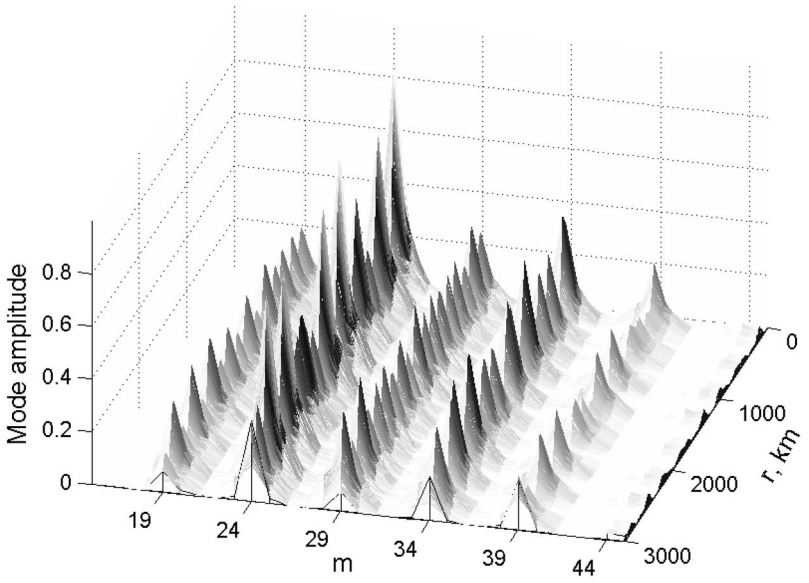

FIG. 4. Mode amplitude as a function of range r and mode number m. At $r=0$ only the 24th mode is excited.

Fig. 3(a) where the Husimi function for $\psi_5(z)$ is plotted. It almost coincides with the Husimi function for $\varphi_5(z)$ (not shown). The Husimi functions for the first 19 eigenfunctions $\psi_m(z)$ have forms of fuzzy closed curves localized within the central island. The larger is m, the greater is the difference between $\psi_m(z)$ and $\varphi_m(z)$ and, correspondingly, the less similar are their Husimi functions. The fuzzy curves corresponding to m approaching 19 repeat the shape of the border of the central island. This is clearly seen in Fig. 3(b) where the Husimi function constructed for $\psi_{18}(z)$ is shown.

Figures 3(a)–3(f) demonstrate that the Husimi distribution functions may have quite different structures. All of them can be divided into two groups: modes formed by contributions from predominantly regular rays and those formed by predominantly chaotic rays. Husimi distributions shown in Figs. 3(a), 3(b), and 3(e) reside on stable islands and therefore the corresponding Floquet modes are regular. In contrast, the modes represented in Figs. 3(c), 3(d), and 3(f) are localized within the chaotic sea and therefore they may be called irregular.

We conjecture that the Husimi distributions closely surrounding the stable islands or sub-islands [e.g. those shown in Fig. 3(c)] represent the finite-wavelength analog to the stickiness—i.e., the presence of such parts of the chaotic ray trajectory where the latter exhibits an almost regular behavior [47]. This occurs when after wandering in the phase space the trajectory approaches a stable island and "sticks" to its border for some time that may be fairly long.

Our division of Floquet modes into the regular and irregular ones agrees with the classification of the Floquet states in quantum systems introduced in Ref. [46]. According to this classification there are three categories of the Floquet states: (i) regular states localized within the stable islands, (ii) chaotic states uniformly distributed over the chaotic sea, and (iii) states supported by the chaotic sea but localized near the boundary of the stable islands. The states of the form (iii) are called hierarchical because their presence is closely related to the hierarchical structure of the phase space in the vicinity of the islands. Since Husimi distributions corresponding to the irregular modes observed in our simulation occupy comparatively small portions of the chaotic sea near the borders of the five stable subislands, these modes fall into the category (iii) of the above classification. According to the phase portrait shown in Fig. 2 it is to be expected that truly chaotic modes are formed by steep rays. Correspondingly these modes should have large numbers m and this explains why we have not observed such modes in our numerical simulation.

C. Coherent properties of wave chaos: Connection between Floquet modes and modes of the unperturbed waveguide

An important aspect of the wave chaos problem is the manifestation of the ray chaos in range variations of the modal structure of the wave field. This issue was addressed in Ref. [27] using the same environmental model as that considered in the present section. In Ref. [27] we decomposed the wave field into a sum of eigenfunctions $\varphi_m(z)$ and studied range dependencies of mode amplitudes. It was observed that in spite of the ray chaos the modal structure demonstrated surprisingly coherent features. This is seen in Fig. 4 where we have reproduced a result obtained in Ref. [27]. The initially excited 24th mode breaks up into a group of modes. The group turns out to be unexpectedly stable. Modes with numbers 19, 24, 29, 34, and 39 strongly dominate at any range $r \gtrsim 100$ km. Mode amplitudes are normalized so that $B_{24}(0)=1$. In Ref. [27] this effect was qualitatively interpreted from the viewpoint of the mode-medium resonance responsible for strong coupling of modes whose horizontal wave numbers satisfy the resonance conditions. Using the Floquet theory we can obtain an additional insight into this phenomenon and look at the mode-medium resonance from a new viewpoint.

Figure 5 shows absolute values of C_{qm}, dimensionless coefficients in the decomposition (44). As has been indicated above the mth column of matrix $\|C_{qm}\|$ defines the mth Floquet modes. The upper panel of Fig. 6 graphs the dependence

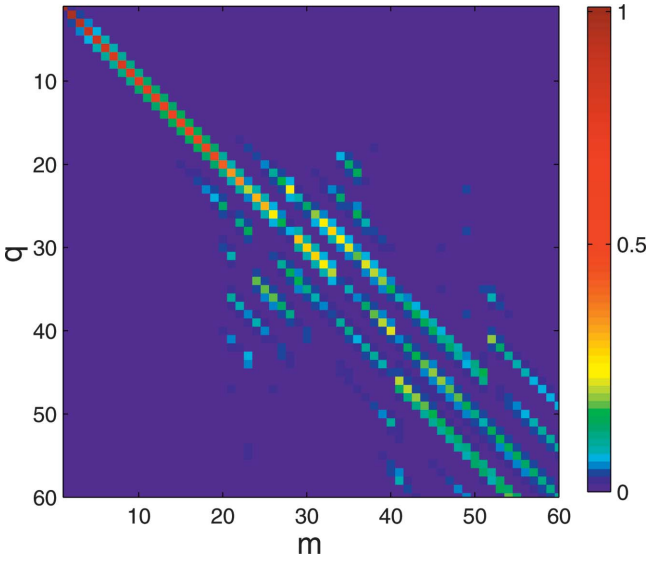

FIG. 5. (Color) Absolute values of coefficients C_{qm} determining decomposition (44).

of parameter μ defined by Eq. (45). The dependence of μ on m is not absolutely monotonic. When numbering the Floquet modes we have slightly broken the monotony in order to make the pattern presented in Fig. 5 as regular as possible. As a result we see that the off-diagonal elements of matrix $\|C_{qm}\|$ form bright stripes parallel to the main diagonal in Fig. 5. The presence of these stripes reflects the fact that the quantity $|C_{qm}|$ as a function of m has maxima spaced apart by 5 for $q \lesssim 40$. The spacing between maxima changes from 5 to 6 as q approaches 60. This periodicity of maxima explains the structure of the pattern seen in Fig. 4. In the next section we shall consider the perturbation theory that relates the appearance of the maxima to the phenomenon of mode-medium resonance.

The lower panel of Fig. 6 presents an estimate for the number of unperturbed modesd forming the mth Floquet one

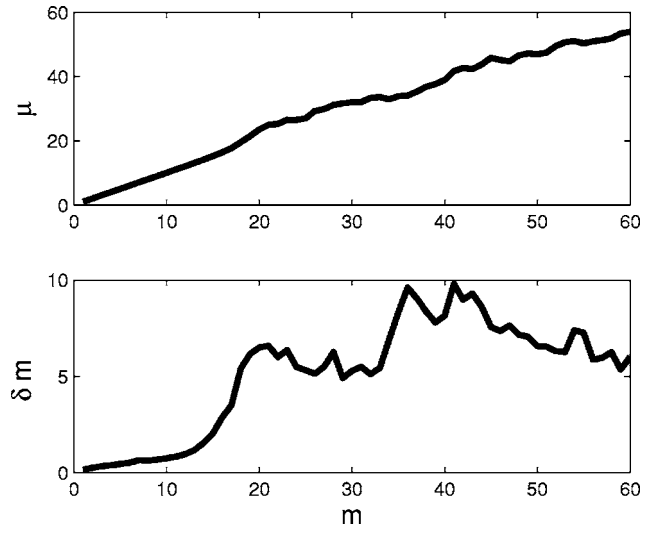

FIG. 6. *Upper panel*: parameter μ [defined by Eq. (45)] associated with the mth Floquet mode. *Lower panel*: the number of unperturbed modes forming the mth Floquet mode, δm, estimated according to Eq. (54).

$$\delta m = \left[\sum_q (\mu - q)^2 |C_{mq}|^2 \right]^{1/2}. \tag{54}$$

This quantity is comparatively small for modes with $m < 20$ whose Husimi functions are localized within the central islands. For other modes the values of δm are significantly larger regardless of whether the mode is "regular" or "irregular". A similar effect was observed in Ref. [48] and called delocalization. We also adopt this term. It emphasizes that typically the Floquet eigenfunction $\psi_m(z)$ consists of many eigenfunctions $\varphi_m(z)$ corresponding to the smooth unperturbed waveguide. Since each $\varphi_m(z)$ represents a superposition of two quasi plane (Brillouin) waves [19], the angular structure of the wave field formed by $\psi_m(z)$ is much more detailed than that of $\varphi_m(z)$. As we shall see in Sec. IV, due to this effect, the Floquet modes are much more sensitive to smooth sound speed variations than the modes of the unperturbed waveguide.

D. Perturbation theory for Floquet modes

Let us derive a simple perturbation theory based on the smallness of δc_{iw} and smoothness of $\bar{c}(z)$ which provides an approximate analytical description of coefficients C_{qm} and gives an additional insight into the role of the mode-medium resonance in connection between the Floquet modes and that of the unperturbed waveguide.

Due to the weakness of perturbation δc_{iw}, the potential $U(r,z)$ in Eq. (4) can be approximately rewritten as

$$U(r,z) = \bar{U}(z) + V(r,z), \tag{55}$$

where

$$V(r,z) = \delta c_{\mathrm{iw}}/c_0. \tag{56}$$

Consider the wave field within the range interval $(0, L)$. Substituting the decomposition (34) into Eq. (4) with U defined by Eq. (55) yields

$$\frac{i}{k}\frac{dB_m}{dr} = E_m B_m + \sum_{m_1} V_{m,m_1} B_{m_1}, \tag{57}$$

where the matrix element $V_{m,m_1}(r)$ is determined by Eq. (36) with $N(z)$ replaced by $V(r,z)$.

Assume that only one mode is excited at $r=0$—i.e.,

$$B_m(0) = \delta_{m,n}. \tag{58}$$

We shall use a perturbation solution to Eq. (57), $B_m(r) = B_m^{(0)}(r) + B_m^{(1)}(r)$, where

$$B_m^{(0)}(r) = \delta_{m,n} e^{-ikE_n r} \tag{59}$$

and

$$B_m^{(1)}(r) = -ike^{-ikE_m r} \int_0^r dr' V_{m,n}(r') e^{ik(E_m - E_n)r'}. \tag{60}$$

According to Eqs. (59) and (60) the elements of the Floquet matrix F can be approximately presented in the form

$$F_{mn} = F_{mn}^{(0)} + F_{mn}^{(1)}, \tag{61}$$

where

$$F_{mn}^{(0)} = \delta_{mn} e^{-ikE_n L} \tag{62}$$

and

$$F_{mn}^{(1)} = -ike^{-ikE_m L} \int_0^L dr\ V_{mn}(r) e^{ik(E_m - E_n)r}. \tag{63}$$

Using the standard perturbation theory for matrices [42] yields the following approximate expressions for the eigenvalues and eigenvectors of F,

$$\beta_m = e^{-ikE_m L} \left[1 - ik \int_0^L dr' V_{mm}(r') \right], \tag{64}$$

$$C_{mm} = 1, \tag{65}$$

and for $m \neq q$,

$$C_{qm} = -\frac{k e^{-ik(E_q - E_m)L/2}}{2 \sin[k(E_q - E_m)L/2)} \int_0^L dr\ V_{qm}(r) e^{ik(E_q - E_m)r}. \tag{66}$$

In our environmental model defined by Eqs. (1)–(7),

$$V(r,z) = \delta c/\bar{c} = \bar{V}(z) \sin(2\pi r/L), \tag{67}$$

where $\bar{V}(z) = -2\gamma z B^{-1} \exp(-2z/B)$. Substituting this into Eq. (66) yields, for $m \neq q$,

$$C_{qm} = \frac{ik}{2} \bar{V}_{qm} \left(\frac{1}{k(E_q - E_m) + 2\pi/L} - \frac{1}{k(E_q - E_m) - 2\pi/L} \right). \tag{68}$$

This result can be further simplified if the carrier frequency is so high that the WKB approximation is valid. Making use of Eq. (29) yields

$$E_q - E_m = (q - m) \frac{2\pi}{kR_m}. \tag{69}$$

Substituting this relation into Eq. (68) and taking into account of Eq. (39) we finally obtain, for $m \neq q$,

$$C_{qm} = \frac{ikR_m L}{8\pi} \bar{V}_{|q-m|}(I_m) \left[\frac{1}{R_m + (q-m)L} + \frac{1}{R_m - (q-m)L} \right], \tag{70}$$

where the symbol $\bar{V}_\nu(I)$ denotes an amplitude at $\cos(\nu\theta)$ in the expansion (23) with $N(z) = \bar{V}(z)$.

According to this result the coefficients C_{qm} may be arbitrarily large if the cycle length R_m is close to an integer multiple of L—that is, if the condition of the mode-medium resonance (an analog to the nonlinear quantum resonance [16]) is met [38,49,50]. In our model R_m monotonically grows with m from 41.8 km for $m=0$ to 52.4 km for $m=60$. The only one-integer multiple of $L=10$ km in this interval is 50 km which corresponds to the 28th mode ($R_{28}=49.9$ km). The applicability of our perturbation theory requires that $|C_{qm}| \ll 1$ for $m \neq q$. Therefore Eqs. (65) and (70) cannot describe quantitatively Floquet modes with numbers close to 28. Numeric simulations have shown that the most accurate predictions of Eqs. (65) and (70) have been obtained for modes with $m < 20$ whose Husimi distributions are localized within the central stable island. Nevertheless, Eq. (70) properly predicts positions of the main maxima in the dependence of $|C_{qm}|$ on q for practically all modes. This is illustrated in Fig. 7. However, it should be noted that while the perturbation theory predicts only three peaks for each mode, Figs. 5 and 7 show that the modes typically have more peaks. In spite of this restriction the perturbation theory demonstrates the connection between the phenomenon of the mode-medium resonance and the structure of the Floquet mode.

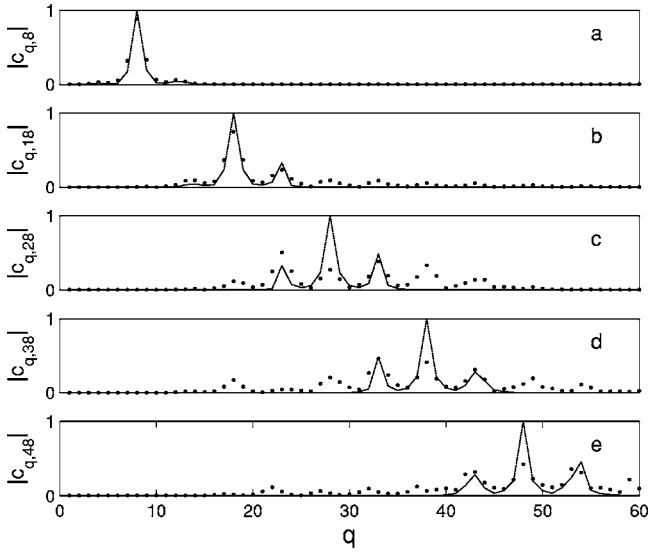

FIG. 7. Coefficients $|C_{qm}|$ found numerically (points) and predicted by Eqs. (65) and (70) (solid lines) as functions of q for $m=8$ (a), $m=18$ (b), $m=28$ (c), $m=38$ (d), and $m=48$ (e).

IV. MODE SCATTERING AT THE SYNOPTIC EDDY

A. Matrices of mode coupling

Let us compare the wave scattering at the synoptic eddy in the presence and absence of the internal-wave-induced perturbation modeled by term δc_{iw}. To this end we have carried out numerical simulations of the wave field within the range interval from 0 to 1000 km in the presence of the eddy whose center is set at range $r_1=500$ km [see Eq. (8)]. The parabolic equation (4) has been solved for two models of the sound speed field. In the first model,

$$c(r,z) = \bar{c}(z) + \delta c_{\text{meso}}(r,z), \tag{71}$$

and we have studied a situation when an incident wave is formed by a single mode of the unperturbed waveguide. The solution of Eq. (4) with an initial condition $u(0,z) = \varphi_m(z)$ has been decomposed into the sum (34). Figures 8(a) and 8(b) describe modal structures of the wave field in cases when initially excited are modes 10 and 24, respectively. The 10th mode restores its amplitude after the eddy which means that this mode varies adiabatically. In contrast, the 24th mode is not adiabatic because it breaks up into a few modes. Figures 8(c) and 8(d) present results of similar calculations car-

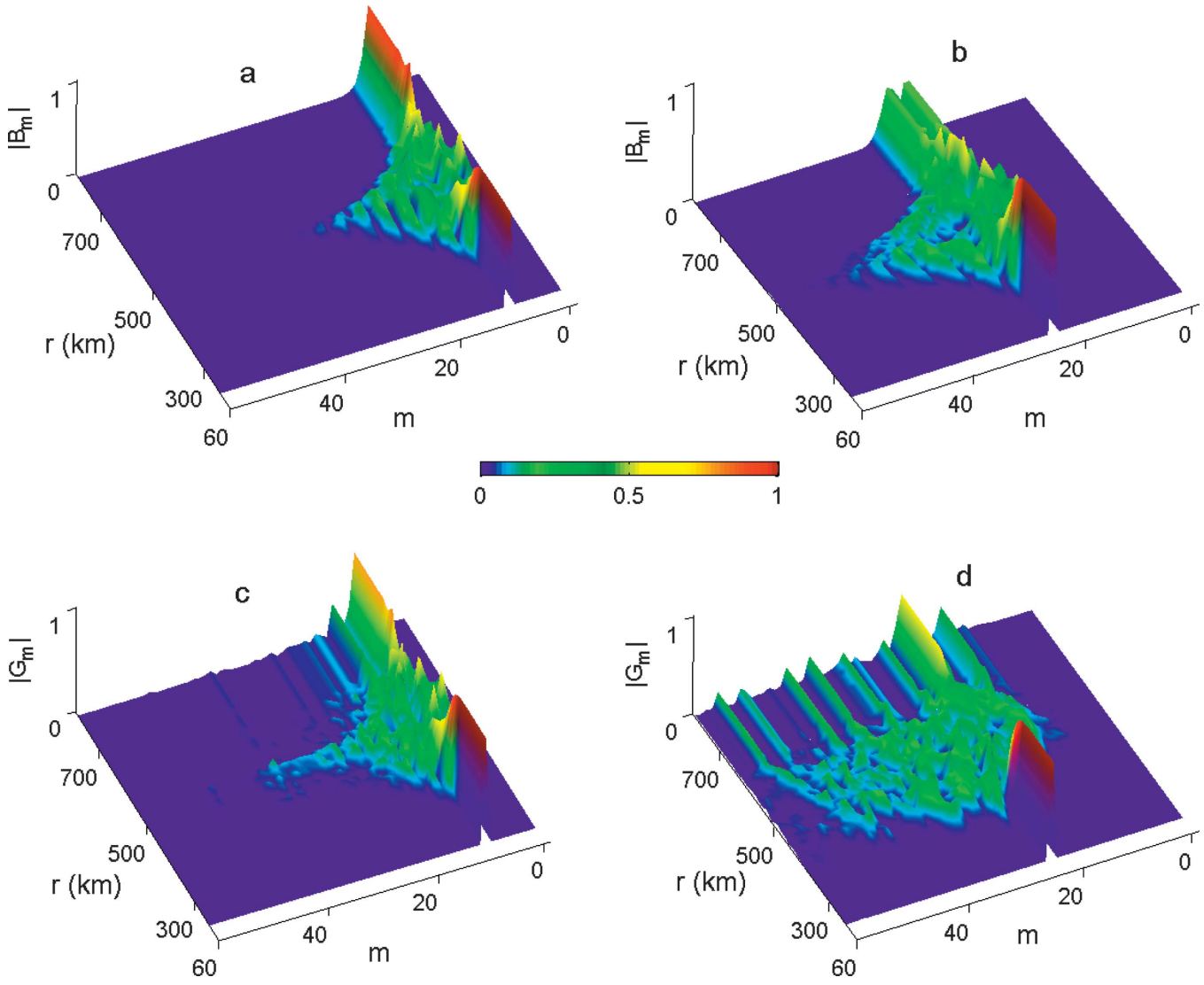

FIG. 8. (Color) Scattering of the 10th and 24th modes of the unperturbed waveguide [(a) and (b), respectively] and Floquet modes with the same numbers [(c) and (d), respectively] at the synoptic eddy. Mode amplitudes are shown as functions of range r and mode number m.

ried out for the environmental model described by Eq. (1) that includes both the internal-wave-induced and mesoscale inhomogeneities. These plots have been constructed by decomposing the wave fields at discreet ranges nL into sums of the Floquet modes. The latter are expressed by Eq. (48) with the coefficients G_m depending (due to the presence of the eddy) on nL. The smooth surfaces shown in Figs. 8(c) and 8(d) approximate dependences of the coefficient $|G_m|$ on discreet arguments m and nL. Again it is assumed that an incident wave is formed by a single mode. But this time it is a Floquet mode. Comparison of the upper and lower rows of plots in Fig. 8 shows that the presence of a weak range-dependent inhomogeneity δc_{iw} modeling the influence of internal wave makes the mode coupling much stronger.

In order to obtain quantitative characteristics of mode coupling at the eddy we shall introduce two matrices Q and P connecting mode amplitudes at $r=-\infty$ (in our computation at $r=0$) and $r=\infty$ (at $r=1000$ km). The matrices are defined by equations

$$B_m(\infty) = \sum_n Q_{mn} B_n(-\infty) \tag{72}$$

and

$$G_m(\infty) = \sum_n P_{mn} G_n(-\infty). \tag{73}$$

They describe mode scattering in the waveguides with the sound speed fields (71) and (1), respectively. The matrices Q and P are shown in the upper and lower panels of Fig. 9. Comparison of these matrices supports the above statement that the internal-wave-induced inhomogeneity giving rise to ray chaos significantly intensifies the mode coupling.

The comparison of matrices Q and P makes sense because average grazing angles of waves forming the mth Floquet mode and the mth mode of the unperturbed waveguide are approximately equal. At the same time, due to the delocalization effect (see Sec. III C1), the angular spectrum of the Floquet mode is significantly wider than that of its un-

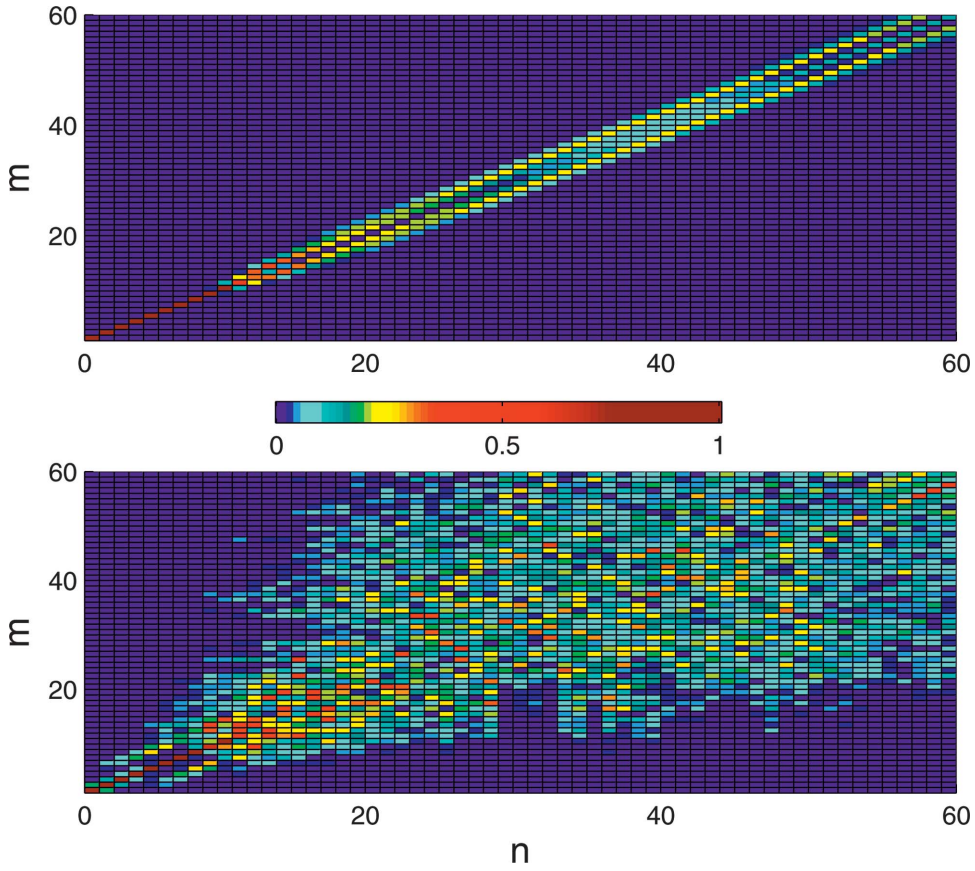

FIG. 9. (Color) Matrix elements $|Q_{mn}|$ (upper panel) and $|P_{mn}|$ (lower panel) determined by Eqs. (72) and (73) and characterizing mode scattering at a synoptic eddy in the absence and presence of perturbation δc_{iw}, respectively.

perturbed counterpart. Angular intervals corresponding to different Floquet modes overlap, and therefore even a smooth inhomogeneity with a narrow scattering indicatrix may cause a strong coupling of Floquet modes. So the high sensitivity of the chaotic-wave field to a smooth mesoscale inhomogeneity is associated with the effect of delocalization.

B. Interaction between "regular" and "irregular" components of the wave field

Results discussed in Sec. III B mean that the total wave field in a waveguide with periodic range dependence may be presented as a sum of "regular" and "irregular" constituents. The regular constituent is a superposition of the regular Floquet modes, and it is formed by contributions from predominantly regular rays. In contrast, the irregular constituent includes hierarchical and chaotic modes. Figures 8 and 9 suggest that the synoptic eddy will cause an interaction of these constituents. A comparison of Husimi distributions computed before and after the eddy (not shown) demonstrates that the wave fields with Husimi distributions localized within the central stable island or five sub islands after scattering at the mesoscale inhomogeneity acquire "irregular" constituents. Naturally, a similar effect takes place for rays. Due to scattering at the eddy, a regular ray may enter the portion of the phase space occupied by the chaotic sea and become chaotic. Vice versa, a chaotic ray may enter the stable island and, thus, become a stable one.

V. VARIATIONS OF THE TIME FRONT

A. Scattering at a synoptic eddy

So far, we have considered manifestations of the ray chaos in the structure of a monochromatic wave field. Now turn our attention to pulse signals. Their structures to a significant extent are determined by the ray travel times T [defined by Eq. (16)] representing arrival times of sound pulses coming to the receiver through individual ray paths [9,19,51]. In many schemes of the acoustic monitoring of ocean structure, ray travel times are the main observables used to reconstruct variations in the environment [21,31,52]. This fact has aroused great interest in their properties. Both numerical simulations and field experiments demonstrate that some features of the distributions of ray travel times in the unperturbed waveguide with a smooth sound speed field may be observed in the presence of a weak perturbation giving rise to ray chaos as well [9,10,33,34]. In the presence of an internal-wave-induced perturbation an original ray connecting the source and receiver breaks up into a group of chaotic rays whose travel times form a rather compact cluster. The center of the cluster is close to the travel time of an original unperturbed ray [10,53,54]. As a result the time front in the perturbed waveguide may resemble that in the unperturbed one. Moreover, some segments of perturbed and unperturbed time fronts may practically coincide.

The results of numerical simulations shown in Fig. 10 demonstrate that in the presence of the synoptic eddy the perturbation δc_{iw}, modeling the influence of internal waves

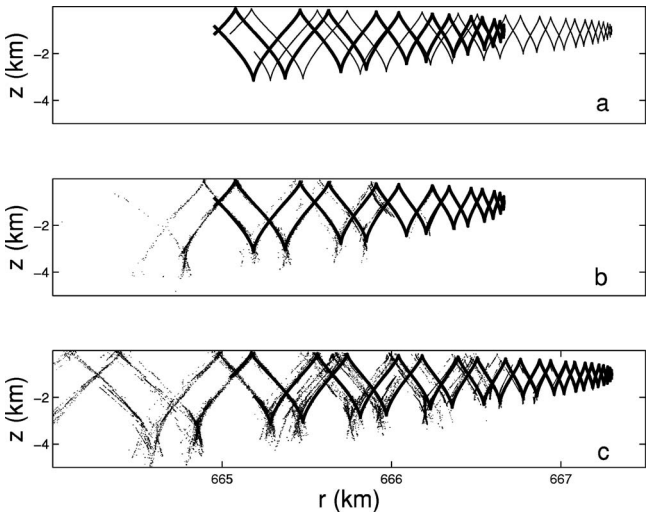

FIG. 10. Time fronts—ray arrivals in the time-depth plane—at the range 1000 km. Rays escape a point source set at a depth of 1 km. (a) Time fronts in the unperturbed waveguide (thick solid curve) and in the presence of a synoptic eddy whose center is placed at $r=500$ km (thin solid curve). (b) Time fronts in the unperturbed waveguide [the same thick solid curve as in (a)] and in the presence of perturbation δc_{iw} (points). (c) Time fronts in the unperturbed waveguide with a synoptic eddy in the absence (solid curve) and presence (points) of perturbation δc_{iw}.

and giving rise to ray chaos, does not destroy the time front as well. In Fig. 10(a) we see how the eddy changes the time front in the absence of internal waves. Figures 10(b) and 10(c) demonstrate that for many segments of the time front the distortion caused by the perturbation δc_{iw} is comparatively weak both in the presence and in the absence of the synoptic eddy. This conclusion is very important from the viewpoint of solving inverse problems. It means that simple formulas relating the time front variations (which may be measured in field experiments) to variations of the sound speed field caused by the mesoscale inhomogeneity (that should be reconstructed) may remain valid even in the presence of internal-wave-induced inhomogeneities giving rise to ray chaos.

Thus, we see that the time front may exhibit comparatively low sensitivity to the internal-wave-induced perturbation δc_{iw} giving rise to ray chaos. In the presence of this perturbation, the mesoscale eddy leads to comparatively smooth and predictable variations of many of the time front segments.

B. Scattering at a rigid bar

However, it should be emphasized that a relative predictability of travel time variations caused by our smooth mesoscale inhomogeneity seen in Fig. 10 is not a general property of the time front under conditions of ray chaos. This statement will be illustrated with a numerical example in which the sound waves propagate in a waveguide shown in the upper panel of Fig. 11. The sound speed in this waveguide is constant, and both boundaries are perfectly reflecting. The upper boundary varies with a range as

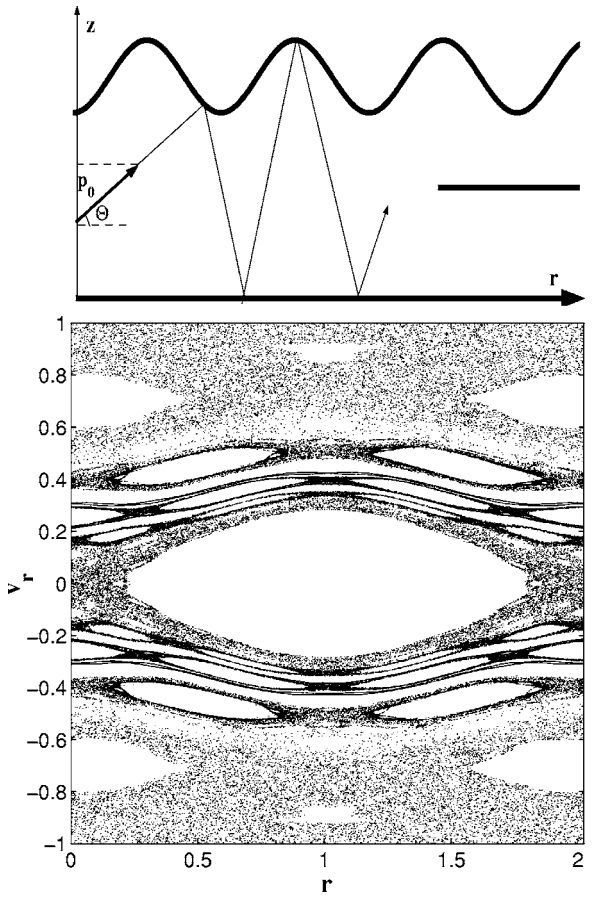

FIG. 11. *Upper panel*: waveguide with a constant sound speed and perfectly reflecting boundaries one of which is a periodic function of range. The scatterer is modeled by a horizontal rigid bar. *Lower panel*: phase portrait of the ray system in the absence of the bar.

$$z = a - b\cos(2\pi r/l),$$

where $a=1$, $b=0.02$, and $l=2$. When describing this waveguide we use dimensionless variables. For simplicity, we take a uniform sound speed c in the waveguide equal to unity. Here we do not use the small-angle (or parabolic equation) approximation, and therefore the momentum $p=\sin\Theta$, where Θ is the ray grazing angle [1,9]. A thin perfectly reflecting bar whose length is equal to $5l$ will play the role of a large-scale scatterer.

First, consider the structure of the phase space in the absence of the bar. A periodic modulation of the upper boundary leads to the ray chaos. This is seen in a phase portrait plotted in the lower panel of Fig. 11. The portrait has been constructed using the map

$$(v_{r,n+1}, r_{n+1}) = \hat{Z}(v_{r,n}, r_n), \tag{74}$$

where the symbol $v_r=\cos\Theta$ denotes a horizontal projection of the wave speed along the ray and $\hat{Z}$ denotes transformation of a pair of ray parameters (r, v_r) at the nth reflection from the lower boundary (bottom) to the $(n+1)$th reflection. Once again we see a typical picture of stable islands submerged in a chaotic sea.

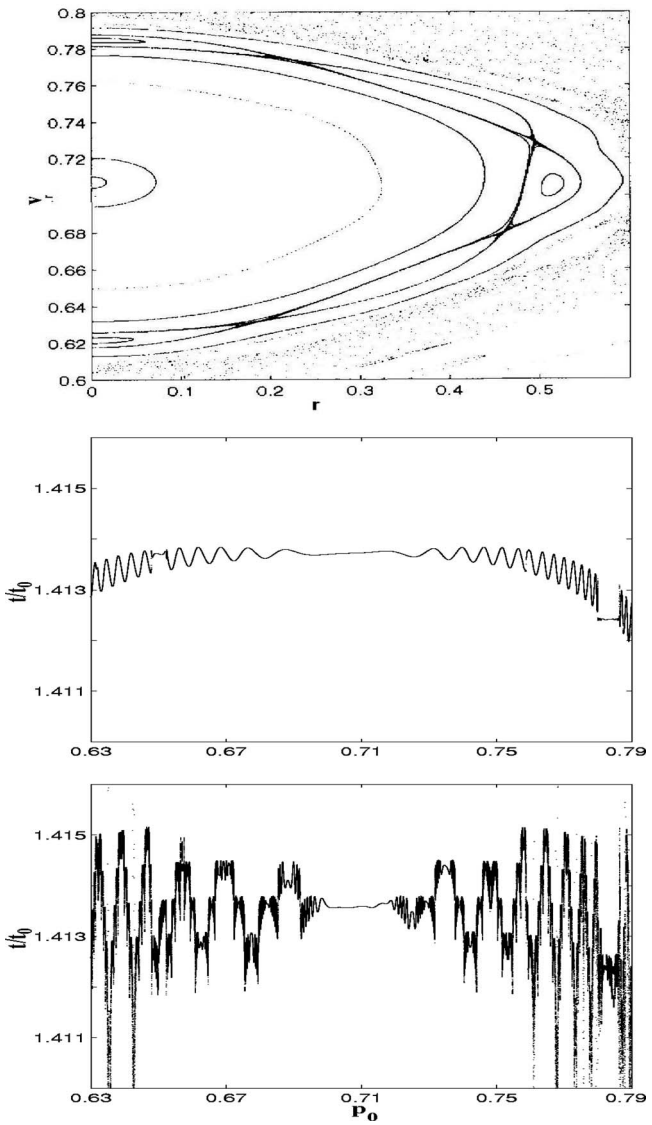

FIG. 12. *Upper panel*: magnified view of a part of the phase portrait shown in Fig. 11. *Middle panel*: ray travel time against starting momentum at range $r=1000$ in the absence of the bar. *Lower panel*: the same as in the middle panel but in the presence of the bar.

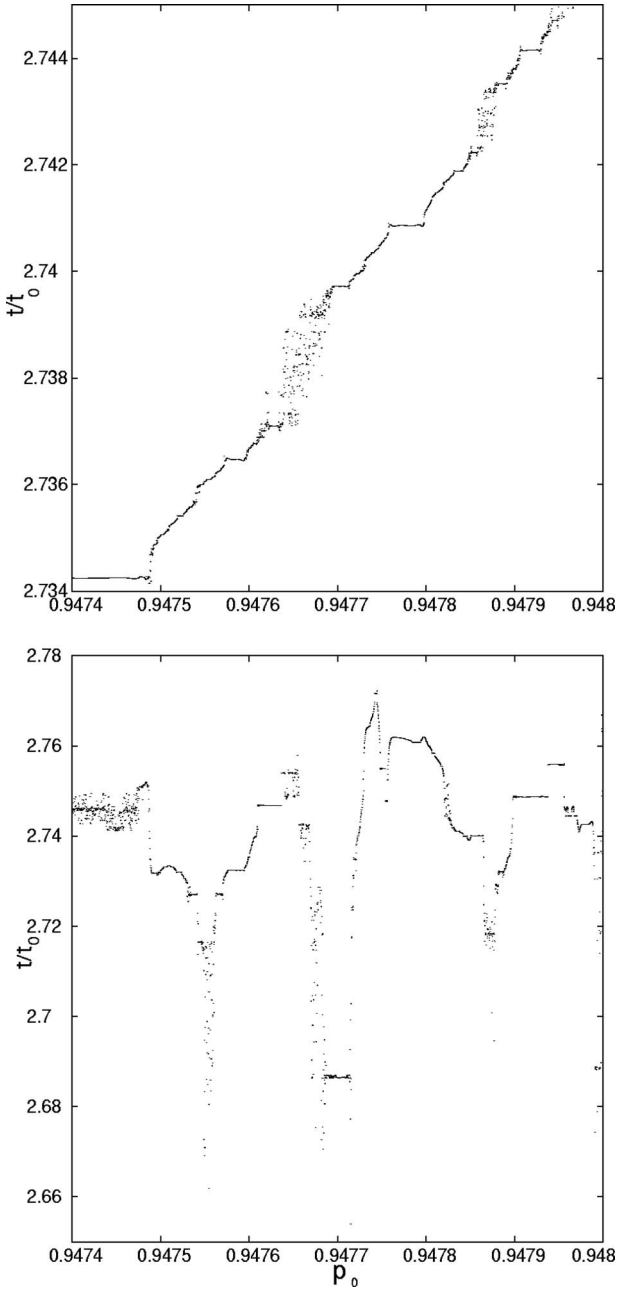

FIG. 13. *Upper panel*: the same as in the middle panel of Fig. 12 but for different intervals of the starting momenta. *Lower panel*: the same as in the lower panel of Fig. 12 but for different intervals of the starting momenta.

The upper panel of Fig. 12 presents a magnified view of a small portion of the phase portrait including a stable island. The middle panel of Fig. 12 graphs the dependence of the ray travel time on the starting momentum p_0 at range $r=1000$ for a point source located at $r=0$ and $z=0$. The travel time t is divided by $t_0=r/c$ representing the arrival time of a pulse signal propagating along the horizontal ray without reflections at the boundaries. The dependence of t/t_0 on starting momentum is shown for rays with starting parameters belonging to the stable island from the upper panel. In the lower panel we see the same dependence in the waveguide with the bar. In our simulations it has been assumed that the center of the bar is set at a range $r=500$ and at a depth $z=0.5$. In the presence of the bar the dependence of t on p_0 becomes less regular and the spread of travel times goes up by a factor of five. This occurs because due to scattering from the bar regular rays may become chaotic. In Fig. 13 a similar comparison is made for steeper rays with starting parameters belonging to the chaotic sea. In the presence of the bar the spread of travel times becomes 10 times greater. Correspondingly, the bar strongly affects the structure of the time front. This is clearly seen in Fig. 14 which demonstrates that the time front in the waveguide with the bar becomes much more chaotic.

It is important to point out that the presence of a perfectly reflecting horizontal bar in the waveguide considered in the preceding sections also makes the time front much more irregular. Figures 15(a) and 15(b) show time fronts at the

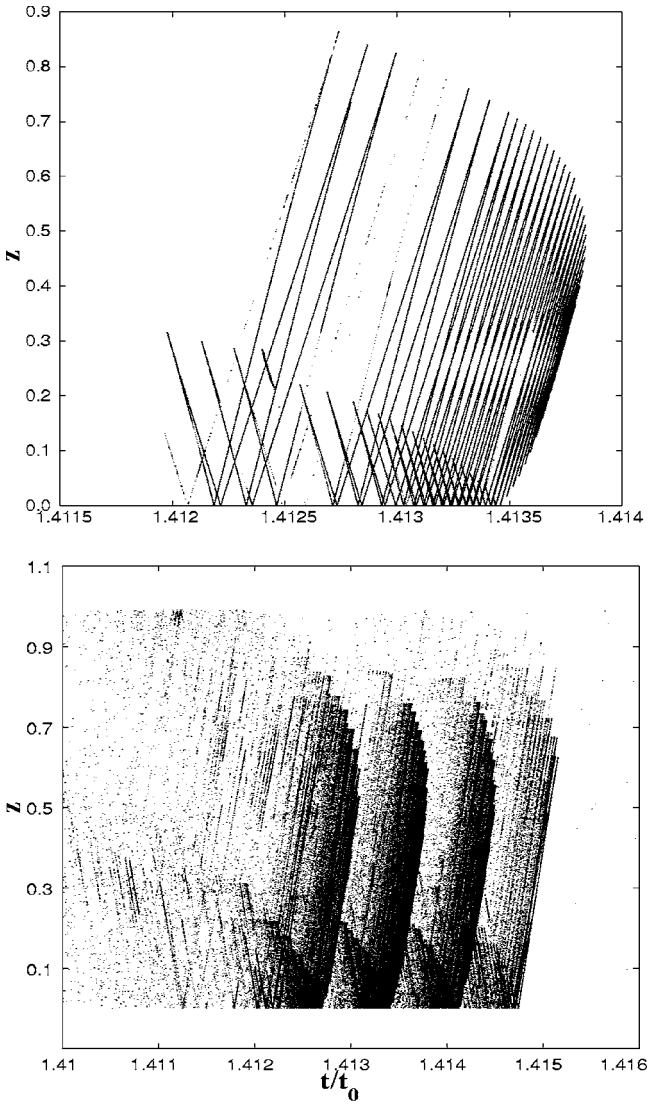

FIG. 14. Time front at range $r=1000$ in the waveguide without (upper panel) and with (lower panel) the bar set at range $r=500$.

range 1000 km computed in the waveguide with the sound speed field determined by Eq. (40) in the absence [the same time front is shown by points in Fig. 10(b)] and the presence of the bar, respectively. The length of the bar has been 50 km and its center has been set at a depth of 1 km at $r=500$ km.

VI. CONCLUSION

In this paper we have considered the properties of wave chaos in a deep-water acoustic waveguide. Our main goal has been to investigate how the mesoscale inhomogeneity affects the wave field. It has been assumed that the chaos is caused by a weak perturbation with a periodic range dependence representing a highly idealized model of environmental variations due to internal waves. The problem has been considered in the parabolic equation approximation. Formally, the wave field in our model is governed by the Schrödinger equation describing a driven quantum system with 1.5 degrees of freedom. A numerical simulation has

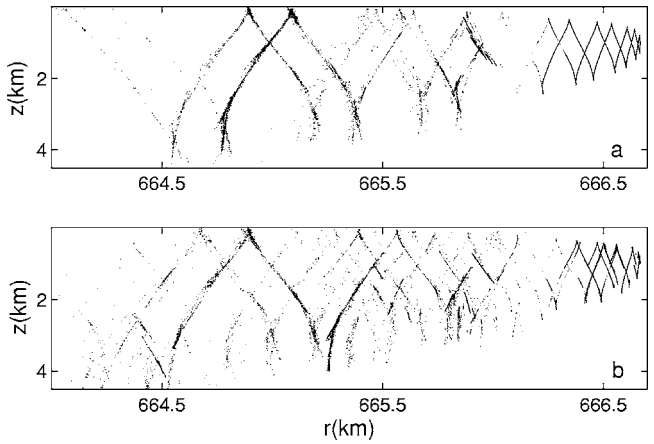

FIG. 15. Time front at range $r=1000$ km in the waveguide medium determined by Eq. (40) without (a) and with (b) a perfectly reflecting bar. The length of the bar is 50 km and its center is set at range $r=500$ km at a depth of 1 km.

demonstrated that the ray trajectories in this system exhibit chaotic motion.

The periodicity of the perturbation greatly simplifies the investigation of both the structure of the phase portrait of the ray system and the structure of the wave field at a finite wavelength. It allows one to exploit the Poincaré map for studying the structure of the phase space of the ray system and the Floquet modes for a description of the wave field at a finite wavelength. It has been observed that the Husimi distributions of the Floquet modes correlate with positions of the stable islands in the phase portrait. Some of the first 60 modes studied in our simulation have the Husimi distributions localized within the stable islands. The Husimi distributions of the remaining modes are localized outside the islands but occupy only comparatively small parts of the chaotic sea. Therefore, in accordance with the classification introduced in Ref. [46] we have observed only regular and hierarchical modes. It may be expected that truly chaotic modes uniformly covering the chaotic sea should propagate at steep grazing angles and have large numbers. This expectation agrees with the structure of the phase space shown in Fig. 2 and with the fact that the perturbation δc_{iw} produces much more irregularity in the distribution of travel times of steep rays than that of flat rays [see Fig. 10(b)].

In our simulation we have considered the wave field at a comparatively low frequency so that the characteristic scales of Husimi distributions are on the order of sizes of the largest islands in the phase portrait. But in reality, in the phase plane there exists an infinite number of smaller islands indiscernible in Fig. 2. At higher frequencies it is natural to expect an appearance of Floquet modes localized not only on large islands but on smaller islands as well.

A simple perturbation theory has been derived that gives approximate analytical relations connecting the Floquet modes to modes of the unperturbed waveguide. This results gives an insight into the role of the mode-medium resonance in mode coupling in the waveguide with a periodic range dependence. It also clarifies the effect observed in Ref. [27], where the perturbed wave field was decomposed into a sum

of modes of the unperturbed waveguide. The perturbation theory gives an approximate quantitative explanation for a surprising periodicity in the dependence of mode amplitudes on the mode number.

In order to study how the properties of wave chaos vary in the presence of a mesoscale inhomogeneity we have simulated the wave scattering at the synoptic eddy. First, we have considered the monochromatic wave field. Since the eddy is rather smooth, it causes only a weak mode coupling in the waveguide without internal waves. But in the perturbed waveguide (with internal waves present) the mode scattering at the same eddy becomes much stronger. Loosely, it may be said that in the presence of weak internal waves giving rise to ray and wave chaos the influence of the eddy on the wave field becomes much stronger.

We have also studied how the eddy affects the time front representing ray arrivals in the time-depth plane. In underwater acoustics it is known that this characteristic to a significant extent determines the structure of the transient wave field. It is also known that although the internal-wave-induced perturbation radically changes individual ray paths making them chaotic, its influence on the time front may be surprisingly small. Our simulation demonstrates that this property of the time front remains valid in the presence of the mesoscale inhomogeneity. This means that variations of the time front caused by the eddy in the unperturbed waveguide may be close to that observed in the presence of internal waves. This conclusion agrees with the fact that methods of acoustic monitoring of mesoscale inhomogeneities derived without taking into account the effects related to the ray chaos prove to be efficient in field experiments [55].

On the other hand, it should be emphasized that the relative predictability of the time front variations caused by a large-scale inhomogeneity is not a general property of the ray chaos. This statement has been illustrated numerically by considering an inhomogeneity in the form of a perfectly reflecting bar.

ACKNOWLEDGMENTS

This work was supported by U.S. Navy Grant Nos. N00014-97-1-0426 and N00014-02-1-0056 and by the Russian Foundation for Basic Research under Grant No. 03-02-17246.

[1] S. S. Abdullaev and G. M. Zaslavsky, Sov. Phys. Usp. **38**, 645 (1991).
[2] D. R. Palmer, M. G. Brown, F. D. Tappert, and H. F. Bezdek, Geophys. Res. Lett. **15**, 569 (1988).
[3] K. B. Smith, M. G. Brown, and F. D. Tappert., J. Acoust. Soc. Am. **91**, 1939 (1992).
[4] S. S. Abdullaev, in *Chaos and Dynamics of Rays in Waveguide Media*, edited by G. Zaslavsky. (Gordon and Breach, New York, 1993).
[5] M. G. Brown, F. D. Tappert, and G. Goñi, Wave Motion **14**, 93 (1991).
[6] F. D. Tappert, M. G. Brown, and G. Goñi, Phys. Lett. A **153**, 181 (1991).
[7] D. R. Palmer, T. M. Georges, and R. M. Jones, Comput. Phys. Commun. **65**, 219 (1991).
[8] M. G. Brown, Nonlinear Processes Geophys. **5**, 69 (1998).
[9] J. Simmen, S. M. Flatté, and G.-Y. Wang, J. Acoust. Soc. Am. **102**, 239 (1997).
[10] F. J. Beron-Vera, M. G. Brown, J. A. Colosi, S. Tomsovic, A. L. Virovlyansky, M. A. Wolfson, and G. M. Zaslavsky, J. Acoust. Soc. Am. **114**, 1226 (2003).
[11] K. B. Smith, M. G. Brown, and F. D. Tappert, J. Acoust. Soc. Am. **91**, 1950 (1992).
[12] M. G. Brown and J. Viechnicki, J. Acoust. Soc. Am. **104**, 2090 (1998).
[13] M. A. Wolfson and F. D. Tappert, J. Acoust. Soc. Am. **107**, 154 (2000).
[14] M. A. Wolfson and S. Tomsovic, J. Acoust. Soc. Am. **109**, 2694 (2001).
[15] A. L. Virovlyansky and G. M. Zaslavsky, Chaos **10**, 211 (2000).
[16] L. E. Reichl, *The Transition to Chaos in Conservative Classical Systems: Quantum Manifestations* (Springer-Verlag, New York, 1992).
[17] M. C. Gutzwiller, *Chaos in Classical and Quantum Mechanics* (Springer-Verlag, New York, 1990).
[18] H. J. Stökman, *Quantum Chaos: An Introduction* (Cambridge University Press, Cambridge, England, 1999).
[19] L. M. Brekhovskikh and Yu. P. Lysanov, *Fundamentals of Ocean Acoustics* (Springer-Verlag, Berlin, 1991).
[20] S. Chin-Bing, D. King, and J. Boid, *Oceanography and Acoustics: Prediction and Propagation Models*, edited by A. R. Robinson and D. Lee (AIP, New York, 1994), pp. 7–49.
[21] W. Munk and C. Wunsch, Deep-Sea Res., Part A **26**, 123 (1979).
[22] S. M. Flatté, R. Dashen, W. M. Munk, K. M. Watson, and F. Zakhariasen, *Sound Transmission through a Fluctuating Ocean* (Cambringe University Press, London, 1979).
[23] E. Ott, *Chaos in Dynamical Systems* (Cambridge University Press, Cambridge, England, 1993).
[24] E. Ott and T. Tél, Chaos **3**, 417 (1993).
[25] I. P. Smirnov, A. L. Virovlyansky, and G. M. Zaslavsky, Phys. Rev. E **64**, 036221 (2001).
[26] I. P. Smirnov, A. L. Virovlyansky, and G. M. Zaslavsky, Chaos **12**, 617 (2002).
[27] I. P. Smirnov, A. L. Virovlyansky, and G. M. Zaslavsky, Chaos **14**, 317 (2004).
[28] A. J. Lichtenberg and M. A. Lieberman, *Regular and Chaotic Dynamics, Applied Mathematical Sciences, Vol. 38* (Springer-Verlag, New York, 1992).
[29] G. M. Zaslavsky, *Physics of Chaos in Hamiltonian Systems* (Imperial College Press, Singapore, 1998).
[30] D. R. Grempel, R. E. Prange, and S. Fishman, Phys. Rev. A **29**, 1639 (1984).
[31] J. Spiesberger and K. Metzger, J. Geophys. Res., [Oceans] **96**, 4869 (1991).

[32] ATOC Consortium, Science **281**, 1327 (1998).
[33] P. F. Worcester, B. D. Cornuelle, M. A. Dzieciuch, W. H. Munk, M. Howe, A. Mercer, R. C. Spindel, J. A. Colosi, K. Metzger, T. Birdsall, and A. B. Baggeroer, J. Acoust. Soc. Am. **105**, 3185 (1999).
[34] J. A. Colosi, E. K. Scheer, S. M. Flatte, B. D. Cornuelle, M. A. Dzieciuch, W. H. Munk, P. F. Worcester, B. M. Howe, J. A. Mercer, R. C. Spindel, K. Metzger, T. Birdsall, and A. B. Baggeroer, J. Acoust. Soc. Am. **105**, 3202 (1999).
[35] L. M. Brekhovskikh and O. A. Godin, *Acoustics of Layered Media. II: Point Sources and Bounded Beams* (Springer-Verlag, Berlin, 1999).
[36] F. B. Jensen, W. A. Kuperman, M. B. Porter, and H. Schmidt, *Computational Ocean Acoustics* (AIP, Woodbury, New York, 1994).
[37] G. M. Zaslavsky and S. S. Abdullaev, Chaos **7**, 182 (1997).
[38] A. L. Virovlyansky, A. Yu. Kazarova, and L. Ya. Lyubavin, Acoust. Phys. **50**, 20 (2004).
[39] L. D. Landau and E. M. Lifshitz, *Mechanics* (Pergamon Press, Oxford, 1976).
[40] M. Born and E. Wolf, *Principles of Optics* (Pergamon Press, Oxford, 1968).
[41] M. C. Gutzwiller, J. Math. Phys. **8**, 1979 (1967).
[42] L. D. Landau and E. M. Lifshitz, *Quantum Mechanics* (Pergamon Press, Oxford, 1977).
[43] K. B. Smith, J. Comput. Acoust. **9**, 243 (2001).
[44] V. I. Tatarskii, Sov. Phys. Usp. **26**, 311 1983.
[45] B. Sundaram and G. M. Zaslavsky, Chaos **9**, 483 (1999).
[46] R. Ketzmerick, L. Hufnagel, F. Steinbach, and M. Weiss, Phys. Rev. Lett. **85**, 1214 (2000).
[47] G. M. Zaslavsky, M. Edelman, and B. A. Niyazov, Chaos **7**, 159 (1997).
[48] G. P. Berman and A. R. Kolovsky, Sov. Phys. Usp. **35**, 303 (1992).
[49] A. L. Virovlyansky and G. M. Zaslavsky, Phys. Rev. E **59**, 1656 (1999).
[50] A. L. Virovlyansky, J. Acoust. Soc. Am. **108**, 84 (2000).
[51] B. D. Dushaw, B. M. Howe, J. A. Mercer, R. C. Spindel, and the ATOC Group, IEEE J. Ocean. Eng. **24**, 202 (1999).
[52] B. D. Dushaw, IEEE J. Ocean. Eng. **24**, 215 (1999).
[53] A. L. Virovlyansky, J. Acoust. Soc. Am. **113**, 2523 (2003).
[54] F. J. Beron-Vera and M. G. Brown, J. Acoust. Soc. Am. **115**, 1068 (2004).
[55] D. W. Behringer, T. Birdsall, M. Brown, B. Cornuelle, R. Heinmiller, R. A. Knox, K. Metzger, W. Munk, J. L. Spiesberger, R. Spindel, D. Webb, P. F. Worcester, and C. A. Wunsch, Nature (London) **299**, 121 (1982).